Chapter 7

Curved vs. flat collector designs: A comparative analysis

In this chapter, we report the investigation of various curved solar air heater designs that shows significant enhancement of heat transfer. We have taken the initial design proposed in the reference: Mahboub, C., Moummi, N., Brima, A., Moummi, A., 2015. Experimental study of new solar air heater design. International Journal of Green Energy 13, 521-529, and incorporated promising design modifications to further look for the avenues for thermal efficiency enhancement features. The Computational Fluid Dynamic (CFD) model was first validated by the results reported by Mahboub et al. It was observed that secondary vortex formation near the absorber wall increases the Nusselt number significantly. New correlations for friction factor and Nusselt number has been developed as a function of Reynolds number and various geometric parameters such as relative groove height and pitch ratios for different design of air heaters. It is hoped that data of parameters i.e. Nusselt number (Nu), outlet air temperature (T_o), thermal efficiency (η_{th}) and friction factor (f) presented in this chapter would help researchers and industry in developing efficient designs of solar collectors.

7.1 Introduction

Growing energy need comes first as a primary requirement to keep the pace of development. Major portion of energy needs are being fulfilled from fossil fuels. However, the major concern arises due to higher prices, environmental pollution, finite reserve and non-replenish nature of fossil fuels such as coal, crude oil, natural resources etc. In today's world a series of research work are running in the sector of renewable energy to get rid of these major drawbacks of fossil fuels. Among all renewable resources such as wind, ocean, tidal, solar, geothermal etc., solar energy is readily available everywhere during the day hours, it is clean, cheap and serves as a tremendous heat source. Harnessing more and more solar energy helps in decreasing the global warming effect on the earth. The solar to thermal conversion of solar energy devices is a key factor but to increase this conversion factor is a major challenge [102].

The conventional flat plate solar air heater (SAH) has been widely used worldwide for solar thermal conversion. A key factor to evaluate the performance of SAH is its thermal efficiency. Various research works has been going on in order to enhance its performance. The transformation of smooth flat rectangular flow channel into curved one as shown in Fig. 7.1(a). The Curved panel show significant increase in the outlet air temperature and, hence thermal efficiency when compared with flat plate SAH, which was experimentally determined in the recent study. Investigations have been carried out for different geometries of absorber plate of SAH i.e. flat plate smooth single pass (FPSP), flat plate smooth double pass (FPDP), curved plate smooth single pass (CPSP), curved plate smooth double pass (CPDP), curved plate semicircular-corrugated single pass (CPSCSP), and curved plate V-corrugated single pass (CPVCSP) solar air heater (SAH). In this chapter, we report further enhancement of performance by incorporating various design changes using Computational Fluid Dynamics (CFD) techniques.

In order to investigate the effect of various design changes on performance, the same initial geometry as shown in Fig. 7.1(a) has been considered for this study.

Many techniques have been investigated to enhance the thermal performance of solar air heater (SAH) by means of protrusion and turbulence promoters but maintaining a balance between cost and effectiveness is a challenge. An economical and high thermal performance SAH having curved shape smooth passage duct was experimentally investigated by [102]. The experimental and theoretical analysis of flat plate, finned and V-corrugated SAH to enhance the thermal performance of conventional air heaters have also been studied [75]. They experimentally investigated the packed-bed SAH with an objective to increase the thermo-hydraulic performance and found that the thermo-hydraulic efficiency decreases with increase in the value of bed depth to element size ratio and bed porosity but it increases with increase in the value of mass flow rates [4]. The experimental and numerical investigation of Dean flow dynamics in low aspect ratio spiral microchannels and effects of secondary flows in curvilinear channel geometries have also been studied [113]. The numerical investigation of SAH duct having roughened with conical protrusion ribs for different relative height and pitch ratios in the range of $0.020 - 0.044$ and $6 - 12$, respectively have been conducted to study the effect on Nusselt number and friction factor for the Reynolds number in the range of $4000 - 16000$ [10]. The different shape of the ribs on the surface and the flow patterns around roughness elements to predict enhancement rate in the thermal performance of SAH have been discussed [155].

There are many studies based on the thermal performance of a flat plate solar air collector with single and multiple pass flow incorporated with thermal energy storage to increase the working hours [19]. The thermal performance enhancement of a convective SAH with provision of pin protrusions on the absorber surface has been performed [53]. The objective behind these investigations were to enhance the heat transfer rate by increasing the surface area of the absorber plate. The increasing trend in the thermal performance of the solar air collector have been found for different flow stream trends incorporated with V-groove [97, 98, 65, 90, 78], helical fins [100], rectangular baffles [29], wire mesh [15], inclined ribs [24], phase change material (PCM) and pin fins equipped with PCM (as a thermal storage) [87, 92] to increase the working duration after sunset were reported. The enhancement of heat transfer in the air flow through impingement jets incorporated with multiple protrusion arc and C-shaped obstacles on absorber plate of solar air heater for various relative roughness height and roughness width [108, 143, 120, 87]. The thermohydraulic and thermal performance of offset finned SAH have been reported in a parametric study for various variable parameters i.e. fin height, air mass flow rate and insolation are found to be more effective for decrease in fin spacing and increase in fin height [125]. The effect on heat transfer characteristics i.e. Nusselt number (Nu) and heat transfer coefficient (h) of flat plate have been reported under environmental wind conditions at different tilt and wind incidence angles i.e. α and θ respectively. Results revealed that Nu is not much sensitive to tilt angle α at windward orientation [158].

Design modifications reported in this chapter can be incorporated in manufacturing by adopting methods that does not add much to the cost of material. Fabrication of curved corrugated absorber plate do not require any special technique. The aim of design modifications is to enhance the turbulence rate in the flow in order to achieve high heat transfer rate from absorber plate to flowing fluid. Correlations have been developed and discussed for Nusselt number and friction factor by using numerical data.

The present chapter is organized as follows: In section 2, details of computational model with boundary condition details about incident solar radiation on the curved SAH and its thermal efficiency (section 3) are discusses. The validation part is described in the section 4, followed by results and discussion in section 5. The correlations for Nusselt number and friction factor have been discussed in section 6 and the conclusion is presented in section 7.

7.2 Description of computational model

CFD analysis of modern curved solar air heater (SAH) model shown in Fig. 7.1(b) having same dimension as that of experimental model considered in the literature [102](Mahboub et al., 2015) (see Fig. 7.1(a)) has been carried out using numerical simulations opting finite volume method for all different geometries considered in the present work. The effect on thermal characteristics for different designs configuration of SAH have been investigated. The methodology adopted for solid geometry, mesh model, computational flow domain, necessary boundary conditions, selection of flow models, properties of flow and validation of results have been discussed in the next section.

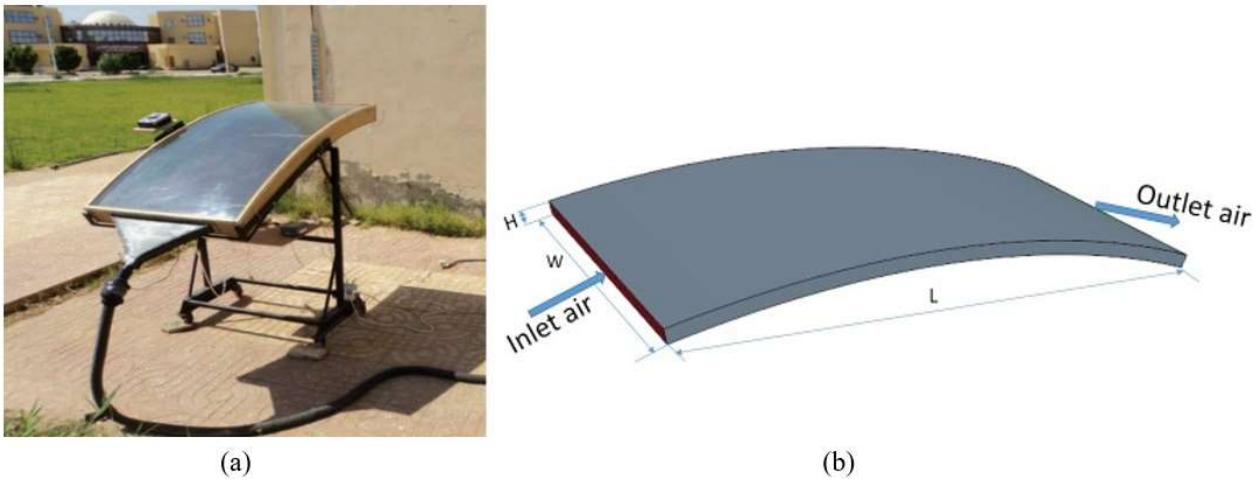

Figure 7.1: (a) Experimental setup [1]; (b) Solid geometry of curved plate SAH.

7.2.1 Basic design details of geometry and parameters

The model considered for the computational domain of curved SAH having rectangular cross-section throughout along the passage connects inlet and outlet respectively. The dimension of length, width and height are 1600 mm, 800 mm and 40 mm, respectively and the curvature radius of absorber plate is 3020 mm for all geometries shown in Fig. 7.1(b). The same dimensions were reported as shown in Fig. 1(a) [102].

The CFD analysis using numerical simulations carried out by considering only the core flow section that actually come under investigation i.e. flow passage comprises of absorber plate, bottom plate, air inlet and air outlet in a single pass flow SAH [10]. In double pass flow SAH, the flow passage has been considered same as in single pass flow and the air available at the outlet of single pass flow is directed into the passage in between glass glazing and absorber plate. Consequently, more heat get collected by the air stream as comes in contact with hot absorber plate exposed to uniform heat flux (q). Investigation has been carried out for different geometries of absorber plate of SAH i.e. flat plate smooth single pass (FPSP), flat plate smooth double pass (FPDP), curved plate smooth single pass (CPSP), curved plate smooth double pass (CPDP), curved plate semicircular-corrugated single pass (CPSCSP), and curved plate V-corrugated single pass (CPVCSP) solar air heater (SAH) as shown in Fig. 7.2(i) and Fig. 7.2(ii). The range corresponds to different relative height and relative pitch ratios of the absorber plate corrugation chosen as 0.125-0.300 and 0.834-3.00, respectively. Simulations for all cases have been performed at three different Reynolds number (Re) whose values are 2209, 3722 and 6058 corresponding to mass flow rate of 0.0172, 0.029 and 0.0472 kg/ s.m^2, respectively. Various parameters are listed in the Table 7.1.

Table 7.1: Range of parameters.

S. No.	Parameters	Parametric values
1	Relative V and semicircular-groove height ratio (e_v/H and e_r/H)	e_v/H = 0.21, 0.3 e_r/H = 0.125
2	Relative V and semicircular-groove pitch ratio (P/ e_v and P/ e_r)	P/ e_v = 0.834, 1.15, 1.25, 1.73 P/ e_r= 2.0, 3.0
3	Reynolds number (Re)	2209, 3722, 6058
4	Mass flow rate (kg/s.m^2)	0.0172, 0.029, 0.0472

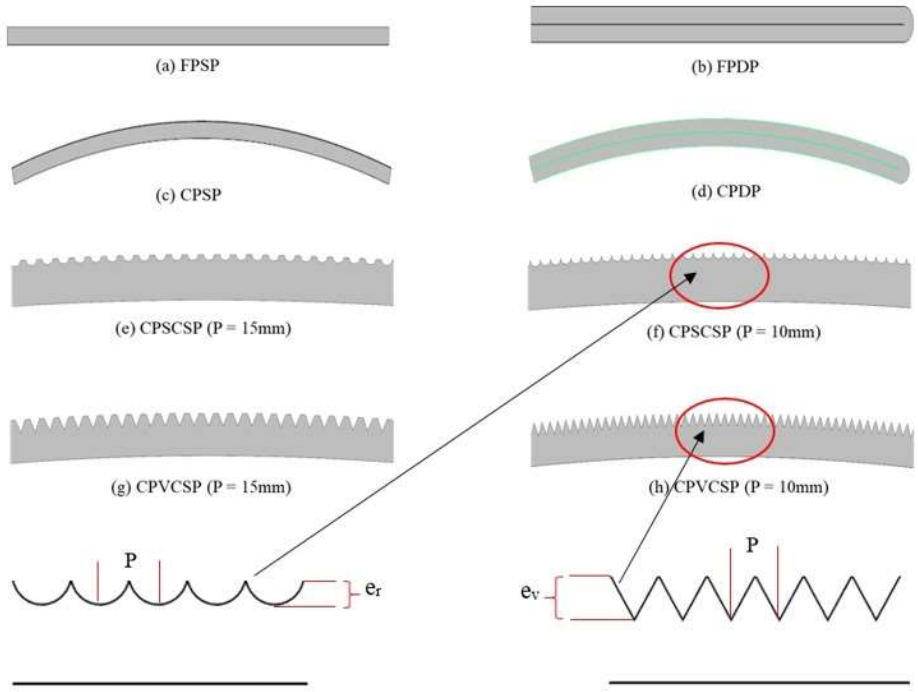

2 (i)

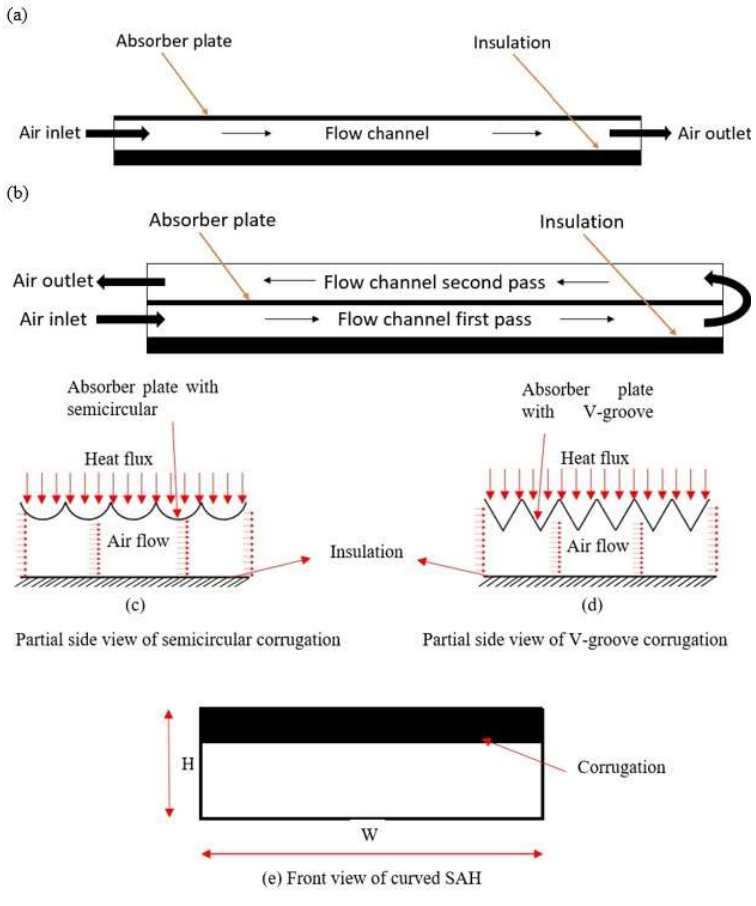

2 (ii)

Figure 7.2: (i) Two-dimensional solid geometry of various curved SAH design. (a) FPSP, (b) FPDP, (c) CPSP, (d) CPDP, (e) CPSCSP (P=15 mm), (f) CPSCSP (P=10 mm) and its magnified view of corrugation, (g) CPVCSP (P=15 mm), and (h) CPVCSP (P=10 mm) and its magnified view of corrugation; (ii) Air flow passage in the duct of curved SAH. (a) Partial side view of single pass flow of curved SAH, (b) Partial side view of double pass flow of curved SAH, (c) Partial side view of semicircular corrugation, (d) Partial side view of V-groove corrugation, (e) Front view of curved SAH.

7.2.2 Methodology of mesh generation and grid independent test of computational domain

The procedure adopted to obtain meshing of SAH model such that to have a balance in between the accuracy of results and less time required to run simulations. Unstructured two-dimensional mesh was created in order to discretize the flow domain for all simulation cases. For more complex geometries an unstructured mesh possess better tendency to capture secondary flow vortices compared to conventional mesh [28]. A fine region of unstructured mesh near the sharp edges of corrugation (grooves) of absorber surface to capture secondary vortex flows. For proper visualization of air flow pattern near the corrugated absorber plate wall, very fine mesh region was generated as shown in Fig. 7.3(a) and Fig. 7.3(b). This helps in predicting the behavior of boundary layer and secondary vortices formation near to the wall of the absorber plate. The dimensionless wall distance (y^+) have been found less than unity.

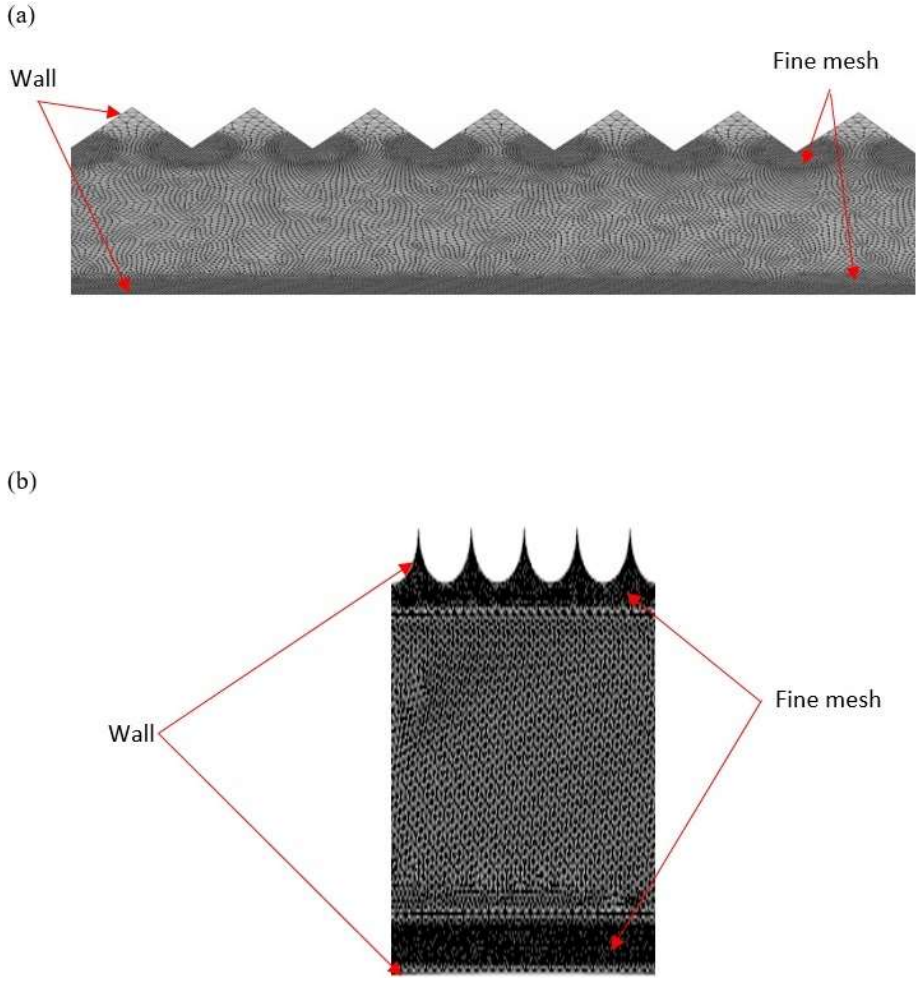

Figure 7.3: Partial view of mesh refinement region near the absorber surface and bottom wall: (a) CPVCSP-SAH and (b) CPSCSP-SAH.

To select appropriate size of the mesh element, grid independent test has been performed for different number of elements in the range of 6.82 x 10^5 to 2.9 x 10^6, respectively for CPVCSP SAH having relative V-groove height (e_v/H = 0.21) and relative pitch ratio (P/ e_v=1.15) at Reynolds number (Re) of 6058. The effect of change in number of elements on the percentage variation of outlet air temperature (T_o) and thermal efficiency (η_{th}) are shown in Table 2. The results obtained after simulation in outlet air temperature (T_o) variation was observed as 1.58% , 0.62% and 0.69% . The corresponding percentage variation in thermal efficiency (η_{th}) was 1.13% , 0.51% and 0.60% as the number of elements increases from 6.82 x 10^5 to 7.27 x 10^5, 7.27 x 10^5 to 1.67 x 10^6 and 1.67 x 10^6 to 2.9 x 10^6, respectively. Since the variations in results is insignificant, the number of elements selected as 1.67 x $10^6$for all further simulation.

Table 7.2: Detail of grid independent test.

S. No.	Number of elements	Percentage variation outlet air temperature (T_o)	Percentage variation in thermal efficiency (η_{th})
1	6.82×10^5	-	-
2	7.27×10^5	1.58	1.13
3	1.67×10^6	0.62	0.51
4	2.90×10^6	0.69	0.60

7.2.3 Boundary conditions

Mesh models of computational flow domain have been generated by taking optimum number of elements by opting finite volume method (FVM) for the discretization. Top wall (absorber plate) of domain was exposed to uniform heat flux of 800, 900, 1000 and 1100 W/m^2. Bottom and side walls of the duct were considered as smooth, adiabatic (no heat loss) and assigned to no-slip boundary condition. The lateral and bottom surfaces were assigned as adiabatic wall similar to the experimental conditions where these surfaces are insulated to avoid heat exchange with the surroundings. Inlet and outlet section of flow domain was set to mass flow inlet (mass flux of air, kg/s.m^2) and pressure outlet (standard ambient pressure taken as reference), respectively. Air possess low thermophysical properties, so for small rise in temperature, all physical properties are assumed to be constant at 300 K temperature throughout the simulation process and listed in Table 7.3.

Table 7.3: Thermo-physical properties of air at 300 K.

Properties name	Value
Dynamic viscosity (μ)	1.855×10^{-5} Ns/m^2
Thermal conductivity (k)	0.026 W/m K
Prandtl number (Pr)	0.71
Specific heat (Cp)	1003.62 J/kg K
Density (ρ)	1.184 kg/m^3

7.2.4 Selection of physics models and governing equations for solution

The flow domain is discretized into very small elements in order to study the air flow movement and heat transfer characteristics using finite volume method. The flow is two-dimensional, steady and incompressible. The $k-\varepsilon$ turbulence model with enhanced wall treatment has been opted during entire numerical analysis. After implementing boundary conditions on the flow domain, the following governing equations i.e. continuity, X and Y momentum, energy, and turbulence dissipation rate ε equations were solved for the two-dimensional numerical analysis. A steady-state numerical analysis using SIMPLE (semi-implicit method for pressure linked equations) algorithm opted to solve velocity and pressure field for the discretized computational flow domain. Convergence criteria has been considered of order 10^{-3} for energy equation and 10^{-5} order for velocity component and momentum equation.

Continuity equation,

$$\frac{\partial \rho}{\partial t} + \nabla \cdot (\rho V) = 0 \tag{7.1}$$

Momentum equations,

$$\frac{\partial (\rho u)}{\partial t} + \nabla \cdot (\rho u V) = -\frac{\partial p}{\partial x} + \mu \nabla (\nabla \cdot u) + \rho g_x \tag{7.2}$$

$$\frac{\partial (\rho v)}{\partial t} + \nabla \cdot (\rho v V) = -\frac{\partial p}{\partial y} + \mu \nabla (\nabla \cdot v) + \rho g_y \tag{7.3}$$

Energy equation,

$$\rho C_p \left(\frac{dT}{dt} + \nabla (TV) \right) = \nabla (\nabla \cdot kT) \tag{7.4}$$

Reynolds number,

$$Re = \frac{\text{Inertia force}}{\text{Viscous force}} = \frac{\rho \, \text{v} \, D_e}{\mu} \tag{7.5}$$

Dean number,

$$D_n = Re\sqrt{\frac{D_H}{R_C}} \tag{7.6}$$

where, $D_H = \frac{H}{2}$ i.e. half of the height of the duct passage of SAH.

The dimensionless parameter i.e. Reynolds number (Re) and Dean number (De) being an important dimensionless parameters to differentiate among laminar and turbulent flow in straight and curved flow duct passage respectively [102, 113]. However, in this present simulation Reynolds numer (Re) and Dean number (De) are in the range of 2209-6058 and 180-494, respectively which comes under turbulent range [102, 113], hence turbulent flow model has been considered during entire simulation run. The SIMPLE (semi-implicit method for pressure linked equations) algorithm is used to solve velocity and pressure field for the discretized computational flow domain. Convergence criteria was set at the order 10^{-3} for energy equation and 10^{-5} order for velocity component and momentum equation.

7.2.5 Global solar radiation and curved collector performance analysis

It will now be shown here that for small curvature of the collector the incident solar radiation is identical to flat collector. The measurement of exact rate of solar irradiation incident on the present curved solar air heater is difficult. An assumption has been considered that the curvature of the curved solar air heater being very small so assumed that it receives global solar radiation similar to flat plate collector having the same collector area. The assumption can be performed by considering the collector area comprises of N surface elements and each surface element dA tilted by an angle β_i with the horizontal receives global solar radiation, could be written as [102]:

$$\mathrm{I}_{\beta i} = I_{hB} \ \left(\cos\beta_i + \tan\theta_z \sin\beta_i \cos\left(\gamma_s - \gamma\right)\right) + I_{hD} \ \frac{1+\cos\beta_i}{2} + I_h \ \rho_g \frac{1-\cos\beta_i}{2} \tag{7.7}$$

Thus, after integrating the above equation over the overall collector area yields average incident solar radiation on the solar collector surface could be evaluated, where $\beta - \phi \leq \beta_i \leq \beta + \phi$, which yields

$$I_\beta = I_{hB} \ \left(\cos\beta + \tan\theta_z \sin\beta \cos\left(\gamma_s - \gamma\right)\right) + I_{hD} \ \frac{1+\cos\beta}{2} + I_h \ \rho_g \frac{1-\cos\beta}{2} \tag{7.8}$$

in which:

$$r = \frac{\sin\phi}{\phi} \tag{7.9}$$

Where, $\phi = \frac{L}{2R_c}$ is the half curvature opening angle and β is the inclination angle at the mid-length point of the surface. For very low values of ϕ, the ratio r tends to unity and the Eq. 7.8 becomes identical to that of solar radiation incident on a plane surface tilted with an inclination angle β.

7.3 Thermal efficiency

The expression used to calculate efficiency of the smooth flat plate collector has been used to evaluate the efficiency of the curved solar air heater in the present work. The quantity of heat captured by air has been seen more in the SAH with corrugated absorber plate compare to simple smooth without corrugation. It is an important task to calculate the thermal efficiency of the duct passage with different geometries of corrugated absorber plate of SAH. The primary parameters for calculating thermal efficiency is the solar insolation that have been incident on the absorber plate, heat gained by the flowing air and various heat losses to environment.

The basic equations that have been required to determine thermal efficiency of solar air heater are given by [39, 150]:

$$Q_u = F_R A_p \left[I\left(\tau\alpha\right) - U_l \left(T_o - T_i\right) \right] \tag{7.10}$$

where F_R is the collector heat-removal factor,
A_p is the area of absorber plate, m^2
U_l is overall heat loss coefficient, W/m^2K
($\tau\alpha$) is transmittance-absorbent product of glass cover

$$F_R = \frac{\dot{m}C_p}{U_l A_p}\left[1 - exp\left\{-\frac{F^{'}U_l A_p}{\dot{m}C_p}\right\}\right] \tag{7.11}$$

where F' is the collector efficiency factor

$$F^{'} = \left(1 + \frac{U_l}{h}\right)^{-1} \tag{7.12}$$

where expression for bottom loss (U_b) , side loss (U_s) and top loss (U_t) coefficients are given as:

$$\mathrm{U}_b = \frac{k_i}{t_i} \qquad and \qquad U_s = \frac{\left(L + W\right) H k_i}{LWt_i} \tag{7.13}$$

$$\mathrm{U}_t = \left[\frac{M}{\left(\frac{C}{T_{pm}}\right)\left(\frac{T_{pm} - T_a}{M+f}\right)^{0.33}} + \frac{1}{h_w}\right]^{-1} + \left[\frac{\sigma\left(T_{pm}^2 + T_a^2\right)\left(T_{pm} + T_a\right)}{\frac{1}{\varepsilon_p + 0.05M(1-\varepsilon_p)} + \frac{(2M+f-1)}{\varepsilon_c} - M}\right] \tag{7.14}$$

where $f = \left(1 - 0.04h_w + 0.0005h_w^2\right)\left(1 + 0.091M\right)$
$C = 365.9\left(1 - 0.00883\beta + 0.0001298\beta^2\right)$
M = number of glass covers
Overall heat loss coefficient (U_l) is sum of side loss, bottom loss and top loss coefficients [39],

$$U_l = U_s + U_b + U_t \tag{7.15}$$

Thermal efficiency (η_{th}) expression is given below:

$$\eta_{th} = \frac{Q_u}{IA_p} = F_R\left\{\left(\tau\alpha\right) - \frac{U_l\left(T_o - T_i\right)}{I}\right\} \tag{7.16}$$

Solar air heater functions on an open cycle in which the atmospheric air is sucked at the inlet section. It is convenient to calculate useful energy gain as a function of outlet air temperature as in Eq. 7.10, instead of considering inlet air temperature because it is equivalent to ambient temperature. Hence the resulting expression of thermal efficiency (η_{th}) is used as it is more practical [102, 4].

7.4 Selection of turbulence model and validation of CFD model

Investigations have been conducted for two-dimensional, steady, and incompressible flow for four different turbulence models, namely; K-Epsilon turbulence, K-Omega turbulence, Spalart-Allmaras turbulence and Reynolds-Stress turbulence. A K-Epsilon turbulence model is a two-equation model that solves transport equations for the turbulent kinetic energy k and its dissipation rate ε . The K-Omega model is two-equation model that solves transport equations for the turbulent kinetic energy k and a quantity called ω , which is defined as the specific dissipation rate, i.e., the dissipation rate per unit turbulent kinetic energy ($\omega \sim \frac{\varepsilon}{k}$). The Spalart-Allmaras model is a low-Reynolds number model, meaning that it is applied without wall functions. According to the formulation of the model, the entire turbulent boundary layer, including the viscous sub-layer, can be accurately resolved and the model can be applied on fine meshes (small values of non-dimensional wall distance y^+). The Reynolds-stress turbulence model, also known as second-moment closure models, solve transport equations for

each component of the Reynolds stress tensor. Comparison of the simulation results of air outlet temperature (T_o) with the experimental results of the previous literature [102] have been used for the validation. The turbulent model that predicts closure values of flow variables with the experimental results was selected for further investigations. Comparison of outlet air temperature (T_o) of all turbulence models for the mass flow rate values of 0.0172, 0.029 and 0.0472 kg/s.m^2 have been presented in Fig. 7.4. The values of outlet air temperature (T_o) were calculated at different Reynolds number (Re) of 6058, 3722 and 2209 when the top absorber surface exposed to uniform heat flux of 800 W/m^2 for K-Epsilon turbulence, K-Omega turbulence, Spalart-Allmaras turbulence and Reynolds-Stress turbulence, respectively. It can be seen that K-Epsilon turbulence model predicts relatively closure values with 0.01% , 2.1% and 6.42% variations with the experimental data as compared to other models. The K-Epsilon model was chosen for high Reynolds number flow which are fully turbulent in nature without separation under moderate adverse pressure gradient.

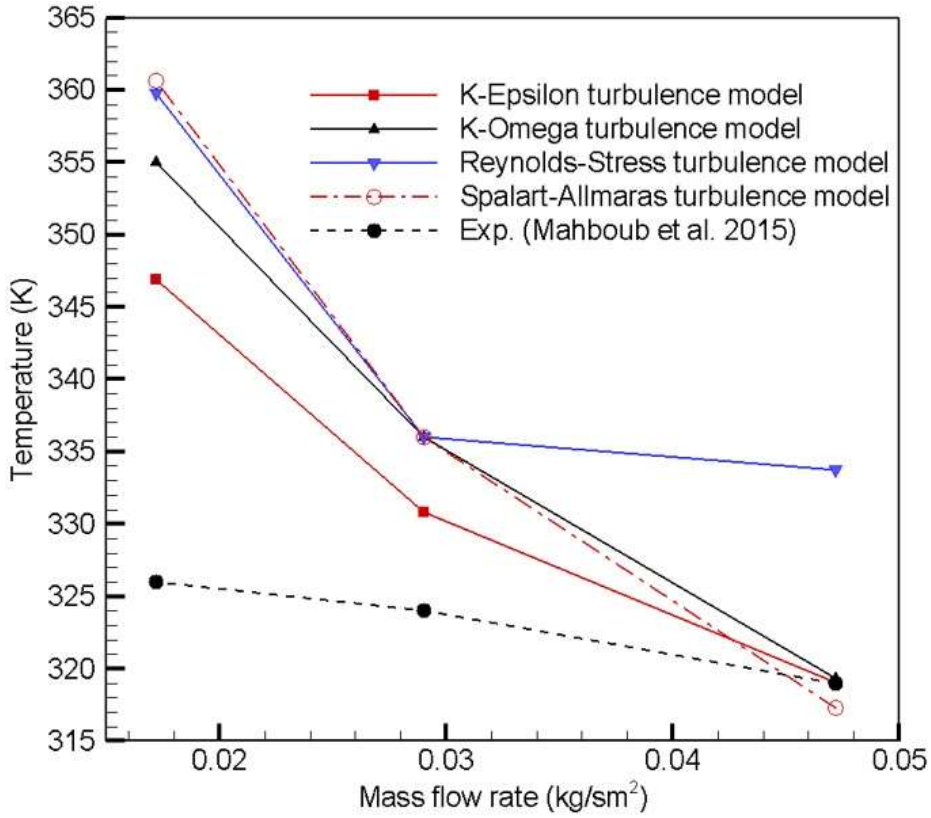

Figure 7.4: Comparison of outlet air temperature (T_o) of different turbulence models with experimental data at different values of mass flow rate i.e. 0.0172, 0.029, 0.0472 kg/sm^2.

The heat losses from the outer surface exposed to the surrounding were assumed to be negligible i.e. adiabatic in simulations, due to which slightly higher values of the outlet air temperature have been found compared to experimental data in the literature [102]. Thermal efficiency of the system was also compared as shown in Fig. 7.5. The percentage variation of thermal efficiency has been found to be in the range of $0.1 - 8.3\%$ at the mass flow rate in the range of $0.0172 - 0.0472$ kg/sm^2. The percentage deviation of 1.85-6.5% has been observed in thermal efficiency with respect to temperature parameter $\frac{To-Ti}{I}$ at the mass flow rate in the range of $0.0172 - 0.0472$ kg/sm^2 (Fig. 7.6). All simulation results that have been discussed above are in good agreement with the experimental results described in the literature [102].

7.5 Results and discussions

The heat transfer characteristics for different geometries of absorber plate of SAH have been obtained for the mass flow rate in the range of $0.0172 - 0.0472$ kg/sm^2 at uniform heat flux in the range of $800 - 1100$ W/m^2. The effect of various geometries of absorber plate on Nusselt number, heat transfer coefficient, outlet air temperature, pressure drop and thermal efficiency have been discussed in this section. The results have been obtained for

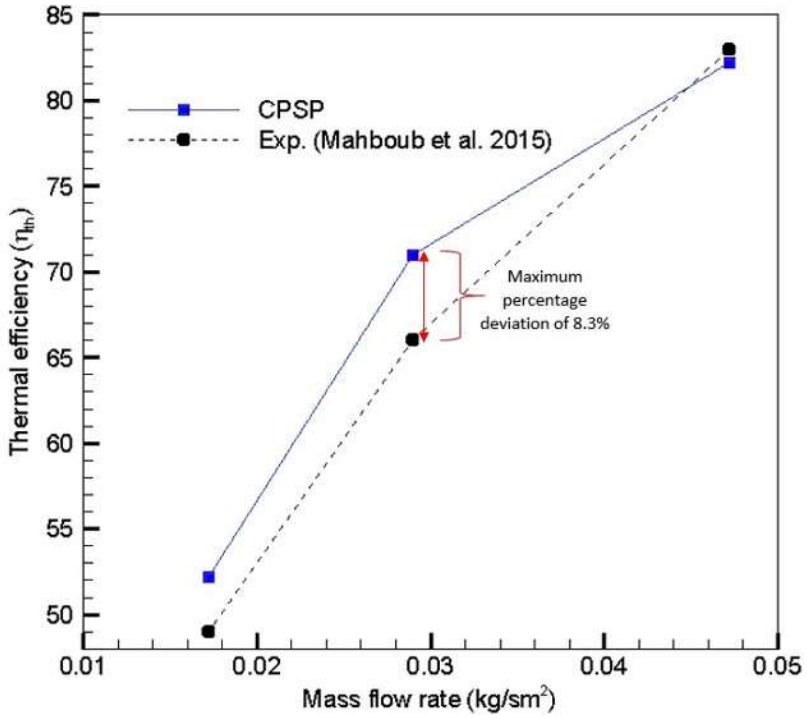

Figure 7.5: Variation in thermal efficiency at mass flow rate of 0.0172, 0.029 and 0.0472 kg/sm^2 under constant absorber heat flux of 800 W/m^2.

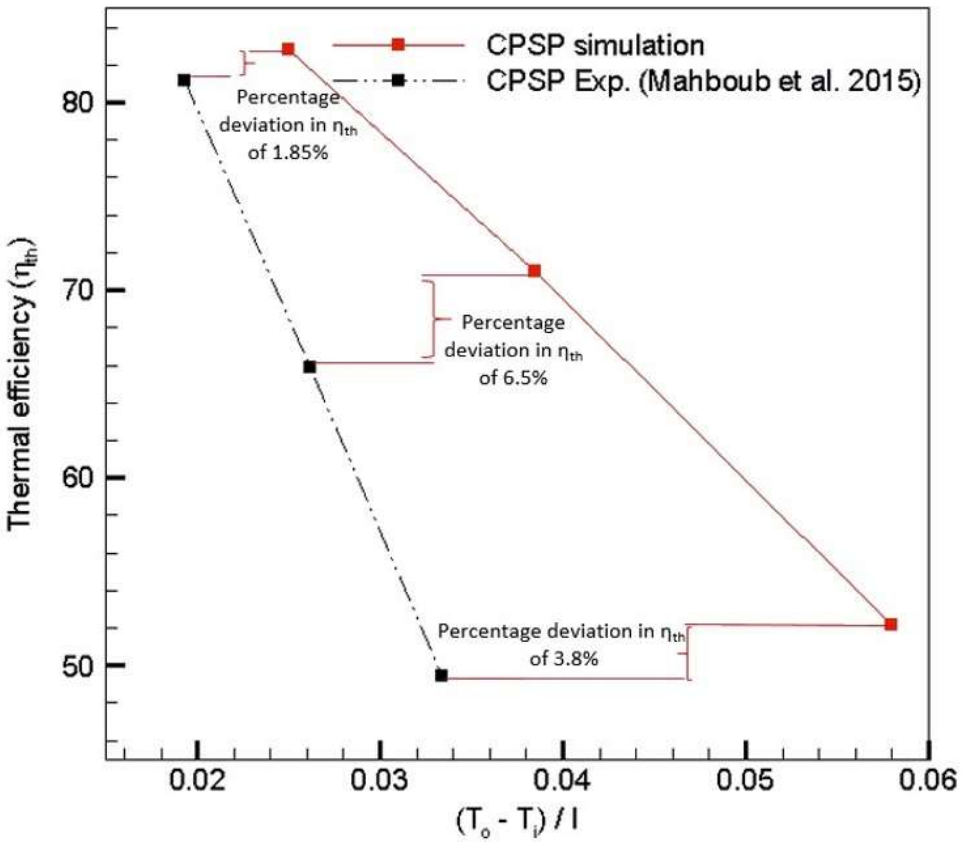

Figure 7.6: Variation in thermal efficiency at mass flow rate of 0.0172, 0.029 and 0.0472 kg/sm^2 under constant absorber heat flux of 800 W/m^2.

all cases and comparisons are made to predict the best geometry of the absorber plate among all geometries that have been considered in the present work. At the inlet of curved plate SAH the entry of air is smooth followed by a curved passage throughout from inlet to outlet section. The centrifugal and centripetal forces comes in picture and plays a very vital role in enhancing the heat transfer rate to the air flowing in the SAH duct. At low mass flow rates centrifugal forces are less intense which does not effects the main velocity profile and consequently formation of small secondary vortices near the absorber plate wall. The increase in the value of mass flow rate i.e. for higher value of Dean number results in increase of the centrifugal force, causing more velocity gradients near the boundaries of the absorber plate.

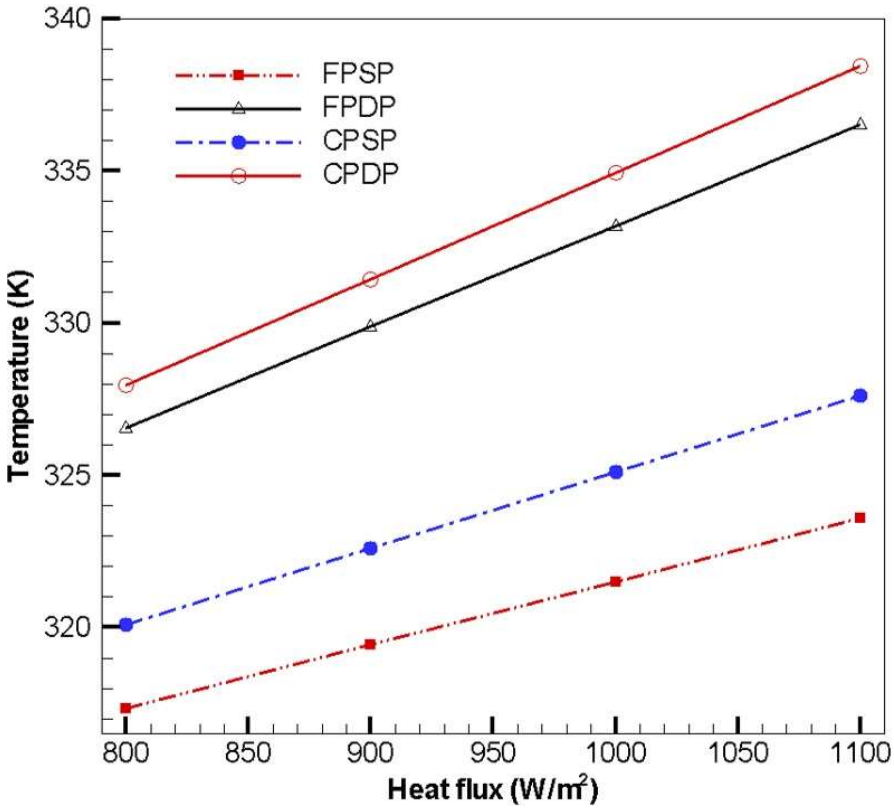

Figure 7.7: Air outlet temperature (To) variation of FPSP, FPDP, CPSP & CPDP SAH w.r.t. absorber heat flux at constant mass flow rate of 0.0472 kg/sm^2.

7.5.1 Effect of different geometries of SAH on heat transfer parameters and thermal efficiency

Figure 7.7 shows the outlet air temperature variation under different heat flux at constant mass flow rate. The corresponding thermal efficiency variation have been plotted for different values of mass flow rate at constant heat flux condition is shown in Fig. 7.8 for various geometries. It can be seen that CPSP SAH shows significant increase in air outlet temperature (T_o) and thermal efficiency (η_{th}) over FPSP SAH. Similarly, to enhance the thermal performance of SAH, CPDP SAH with provision of double pass flow was simulated and found to be more effective than the CPSP and FPDP SAH in respect of air outlet temperature (T_o) rise and thermal efficiency (η_{th}). The enhancement of thermal performance is due to more interaction time of air with the hot absorber plate wall. More pressure drop has been observed in CPSP SAH with percentage increase of 25% than the FPSP SAH, discussed below in detail. This is due to the adverse pressure gradient region near the absorber surface which get compensated by generation of dean vortices.

Due to V-corrugated pattern of the absorber surface in CPVCSP SAH, flow re-attachments on the absorber surface are strong enough to disturb the sub-laminar layer region which give rise to high turbulence in the flow near the absorber wall as shown in Fig 7.16. Similar re-attachment points has also been seen in semi-corrugated absorber surface of CPSCSP SAH but the turbulence intensity being lower, results in lower heat transfer rate compare to the CPVCSP SAH. We observed nearly a linear increasing trend of temperature rise of the air

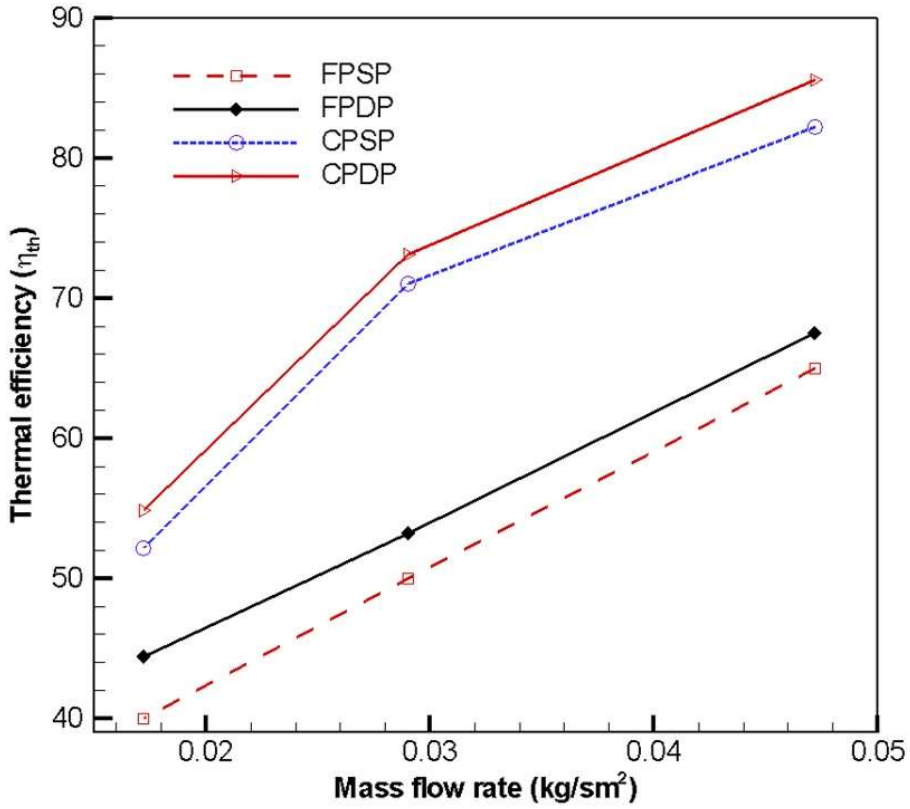

Figure 7.8: Thermal efficiency of FPSP, FPDP, CPSP & CPDP SAH w.r.t. mass flow rate at constant absorber heat flux of 800 W/m^2.

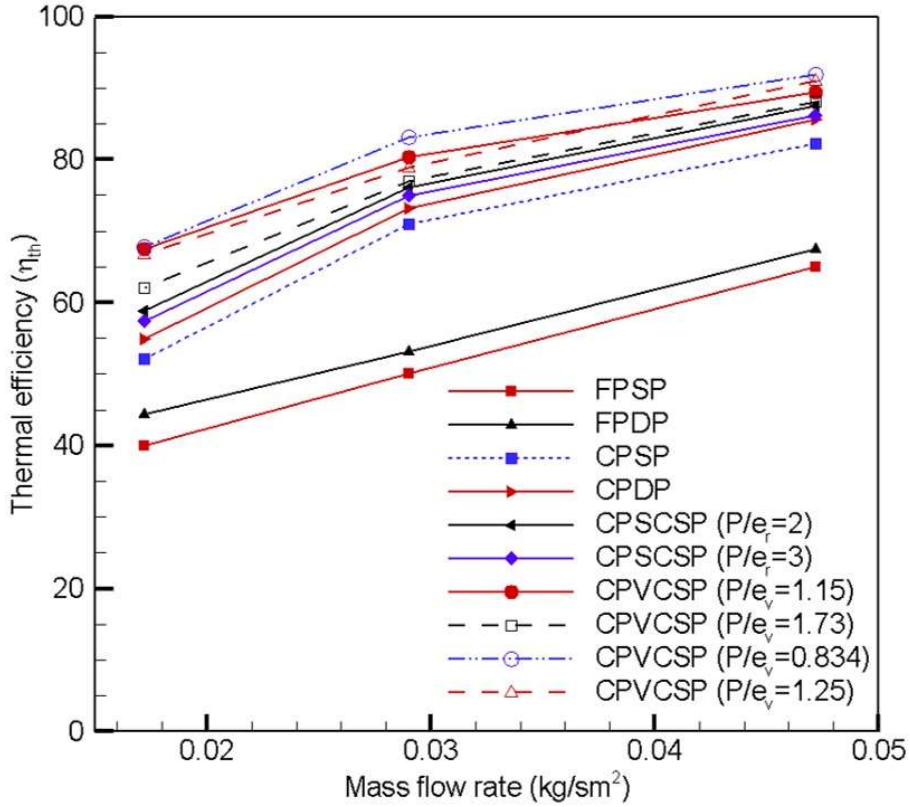

Figure 7.9: Thermal efficiency variation for different geometries of SAH at different mass flow rate values of 0.0172, 0.029, and 0.0472 kg/sm^2.

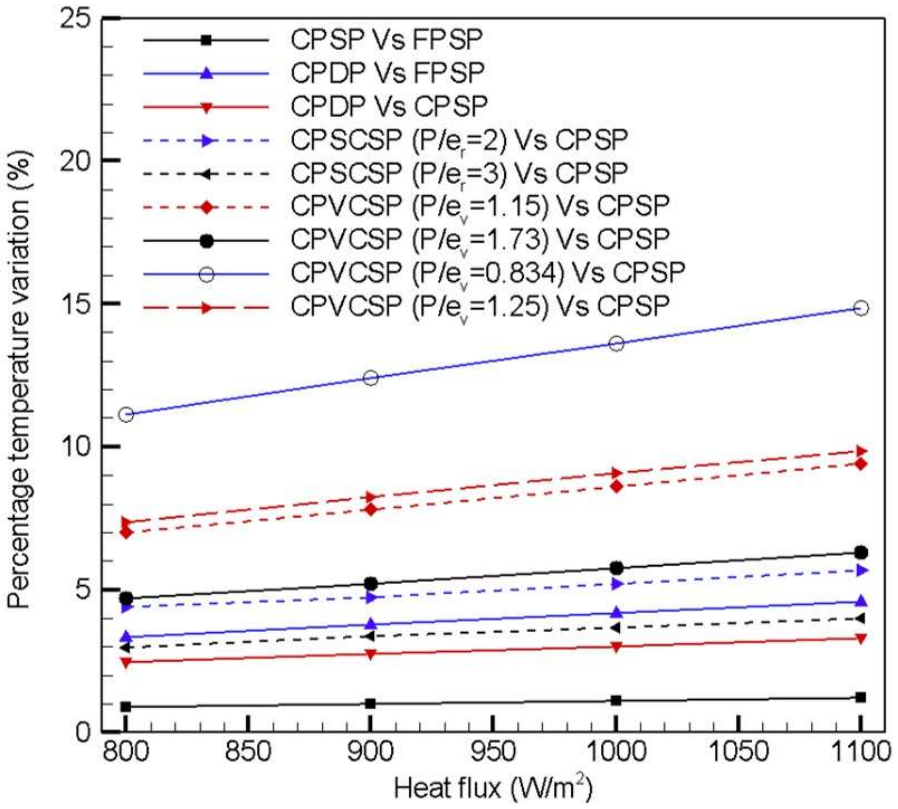

Figure 7.10: Percentage variation of air outlet temperature (T_o) for different geometries of SAH w.r.t. FPSP and CPSP at different values of absorber heat flux.

with increasing heat flux at each value of mass flow rate. The Fig. 7.9 demonstrate the variation of thermal efficiencies for different geometries as a function of mass flow rates. It is notices from the Fig. 7.9 and Fig. 7.10 that among all different geometries of SAH, the CPVCSP SAH shows the maximum percentage increase of thermal efficiency (11.83%) and temperature rise (32.05%) associated with SAH having relative height and pitch ratios of 0.3 and 0.834, respectively. We attribute this due to more surface area and intense mixing of the air due to sharp edge of V-corrugated absorber plate causing more quantity of heat transfer to the flowing air. The percentage variation of air outlet temperature (T_o) for all cases compared with CPSP and FPSP SAH at particular mass flow rate of 0.0472 kg/sm^2 for different values of uniform heat flux have been shown in Fig. 7.10. The maximum temperature was obtained for the CPVCSP SAH having minimum value of relative pitch ratio of P/ e_v= 0.834 due to high turbulence resulting in intense mixing inside the flow. The frequent exposure of fresh air zone with the hot absorber plate wall exaggerate air temperature at the outlet section.

Table 7.4: EAF efficiency augmentation factor.

$\dot{m}$	Efficiency augmentation factor (EAF)					
	P/ e_r=2	P/ e_r=3	P/ e_v=1.15	P/ e_v=1.73	P/ e_v=0.834	P/ e_v=1.25
0.0172	1.129	1.047	1.087	1.070	1.118	1.106
0.029	1.072	1.054	1.130	1.084	1.169	1.109
0.0472	1.064	1.098	1.294	1.189	1.299	1.279

The variation of thermal efficiency for various designs w.r.t. temperature parameter $\frac{To-Ti}{I}$ under uniform absorber heat flux condition is shown in Fig. 7.11. At lower values of mass flow rate, the relatively cold air gets more time to get interact with the hot absorber surface to absorb more heat and effect of which has clearly been seen in the increase of air outlet temperature and vice-versa for higher mass flow rates. The enhancement in thermal efficiency has also been evaluated in terms of efficiency augmentation factor (EAF) which is defined as the ratio of the thermal efficiency of corrugated absorber plate of curved SAH to the curved plate smooth single pass (CPSP) SAH. Efficiency augmentation factor (EAF) for different corrugation in terms of height and pitch of the grooves of curved SAH for different relative pitch ratios of semicircular and V-grooves at mass flow

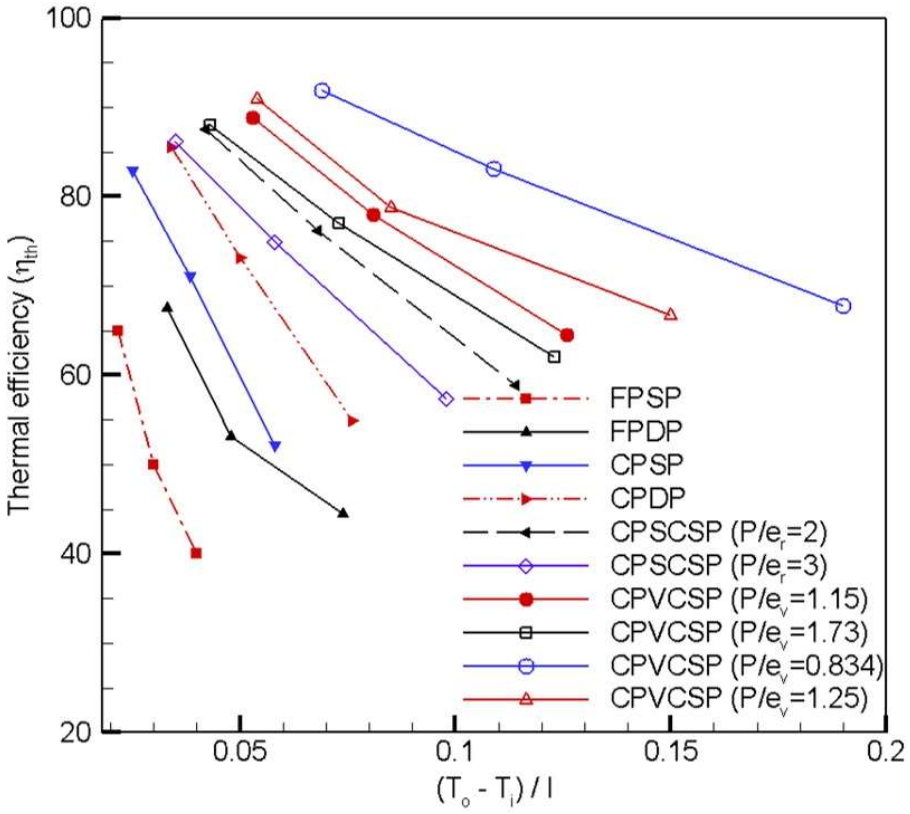

Figure 7.11: Percentage variation of thermal efficiency for different geometries of SAH w.r.t. temperature parameter $\frac{(T_o - T_i)}{I}$.

rate in the range of $0.0172 - 0.0472$ kg/sm^2 has been shown in Table 7.4.

The non-dimensional heat transfer variation in terms of Nusselt number of flow adjacent to absorber plate wall is shown in Fig. 7.12. Positive slope of the variation indicates the increasing trend with mass flow rate. The curved absorber plate with semicircular and V-groove corrugation possess lower values of surface average Nusselt number at the interface of absorber surface and air compare to smooth passage of curved and flat plate SAH without corrugation. The maximum value of surface average Nusselt number is for CPSP SAH due to interaction of continuous flow of air streams with hot absorber wall. In CPDP SAH, at the first pass the heat carrying capacity is more because of large temperature gradient between absorber surface and air, during the second pass gradient value decreases along the flow, and hence yields slightly lower values of Nusselt number. The stagnation state of air being captured in between grooves of corrugated absorber plate is the reason for low values of Nusselt number for curved SAH having semicircular and V-grooves corrugation. A high turbulence zone occurs at sharp tip of the grooves imparts more mixing in the flow which increases the air temperature. The percentage variation of Nusselt number for all different geometries of SAH have been obtained with respect to CPSP and FPSP SAH at different values of heat flux shown in Fig. 7.13.

The pressure drop variation of the flow from inlet to outlet section for all different geometries of SAH at various mass flow rates have been obtained shown in Fig. 7.14. More the obstruction offered to fluid flow correspondingly increases the value of pressure drop. The maximum value of pressure drop obtained for SAH having minimum value of relative pitch ratio i.e. P/e_v=0.834 of the CPVCSP SAH due to more height of the grooves of corrugation. The friction factor (f) being inversely proportional to Reynolds number, increasing trend has been observed with decreasing values of mass flow rate as shown in Fig. 7.15.

7.5.2 Effect of relative height and pitch ratio of corrugation

The relative height and pitch ratio of groove are important parameters in the heat transfer augmentation in case of solar air collectors. Increase in the value of relative height ratio and decrease in the value of relative pitch ratio directly increases the surface area of the absorber plate that has been exposed to air, laterally acting as turbulence creation region near the wall of the absorber plate. Impact of high turbulence region results in

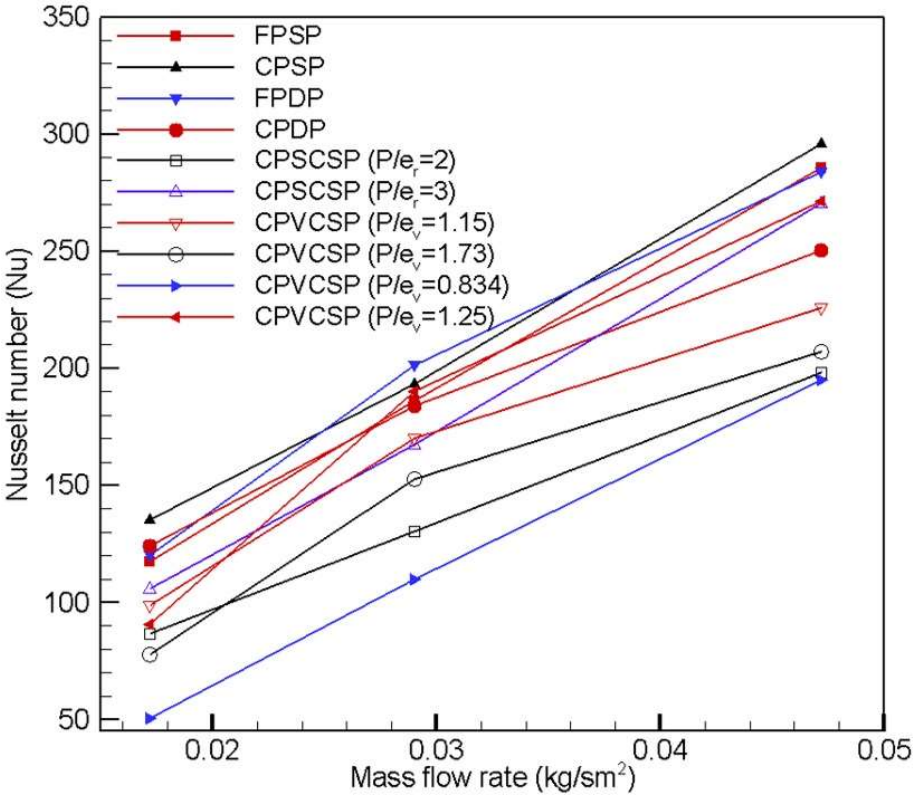

Figure 7.12: Nusselt number variation for different geometries of SAH at each value of mass flow rate i.e. 0.0172, 0.029 and 0.0472 kg/sm2, respectively.

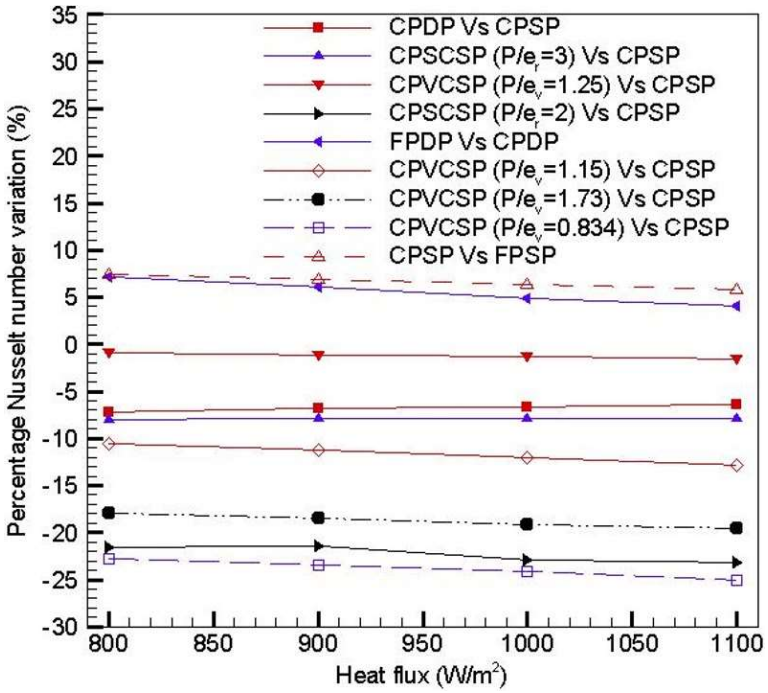

Figure 7.13: Percentage variation of Nusselt number for different geometries of SAH w.r.t. FPSP and CPSP at different values of absorber heat flux.

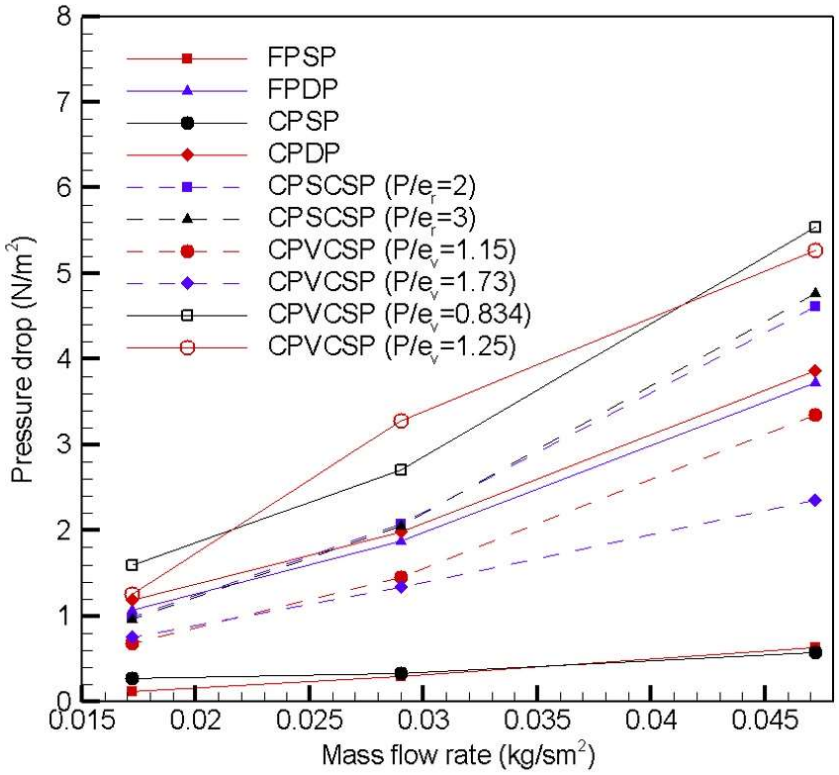

Figure 7.14: Pressure drop variation for different geometries of SAH at each value of mass flow rate i.e. 0.0172, 0.029 and 0.0472 kg/sm2, respectively.

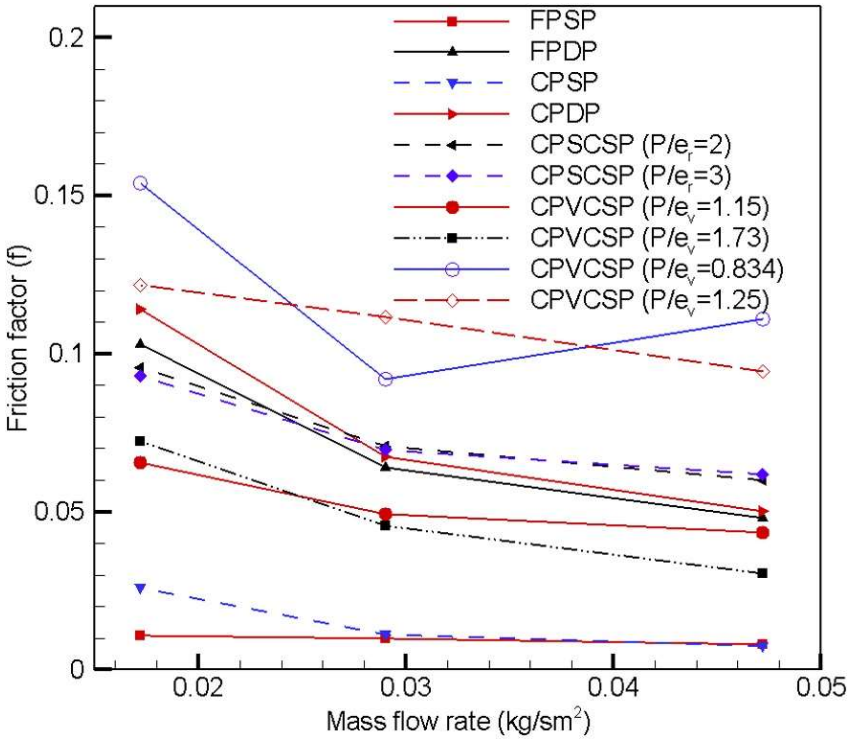

Figure 7.15: Friction factor (f) variation w.r.t. mass flow rate values of 0.0172, 0.029, and 0.0472 kg/sm2.

intense mixing of the fluid particles which helps in mixing fresh air at the center of flow passage with the hot absorber plate. This phenomenon increases the thermal efficiency (η_{th}) by enhancing the heat transfer rate and hence air outlet temperature (T_o). Due to this reason, the CPVCSP SAH offers more thermal efficiency compared to CPSCSP solar air heater, as sharp edges of V-grooves with more height with fine pitch increases the turbulence as shown in Fig. 7.16(a) and (b).

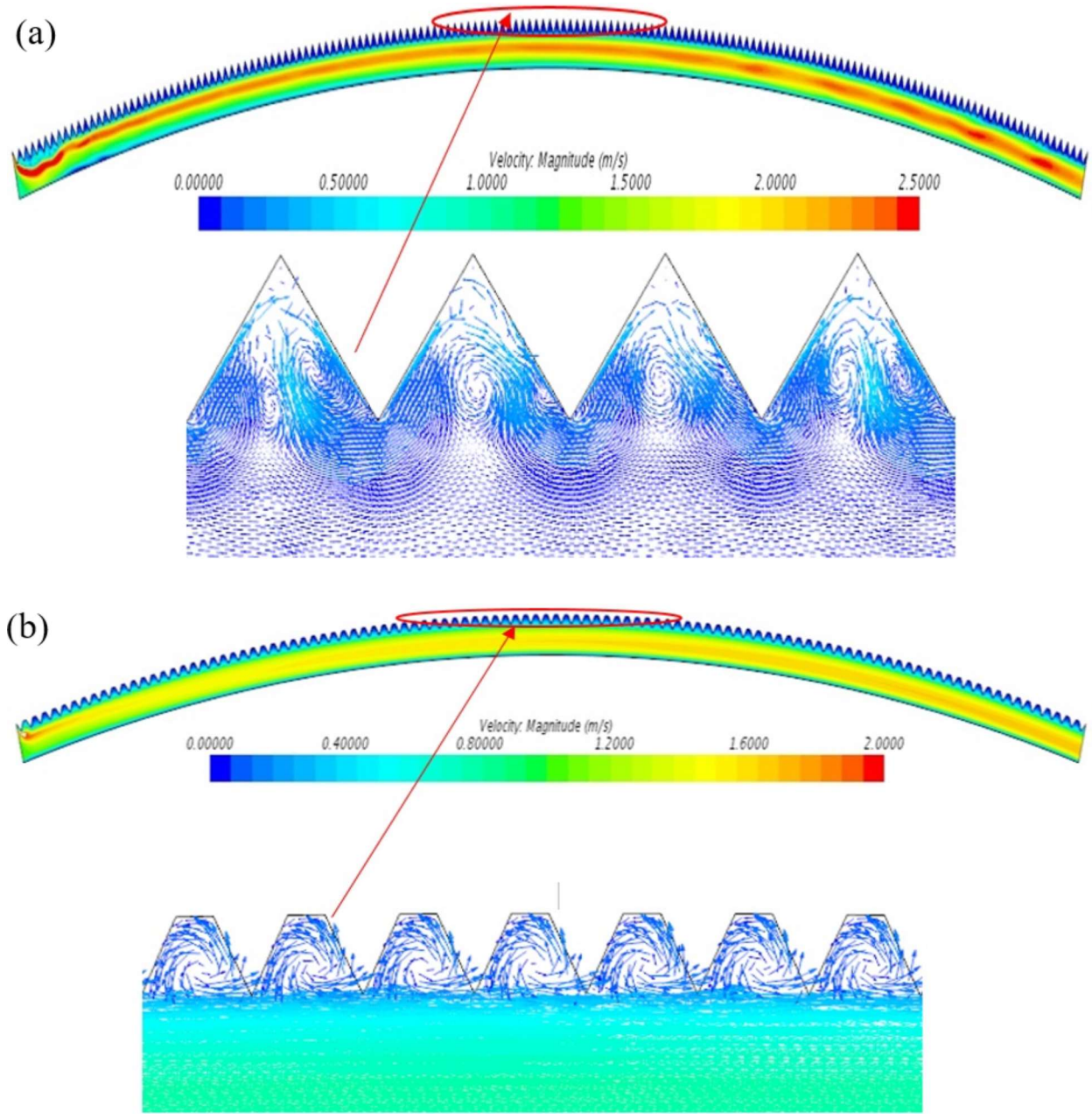

Figure 7.16: (a) and (b) Partial side view of secondary flow vortices formation near the sharp edge of V-grooves having different pitch values of the absorber plate. (a) Velocity contour at the sharp vortex of V-grooves having 10 mm pitch of curved SAH, (b) Velocity contour at the sharp vortex of V-grooves having 15 mm pitch of curved SAH.

The total pressure coefficient i.e. $\left(C_{tp} = \frac{P_o - P_\infty}{\frac{1}{2}\rho V_\infty^2}\right)$, of CPSP SAH is high at the inlet and then it gradually decreases to minimum value at the outlet section due to obstructed flow passage. Here, V_∞ *and* P_∞ are the velocity and pressure of the free stream velocity of the flowing fluid in m/s and N/m^2, respectively. The solar air heater with corrugated absorber plate possess more value of total pressure coefficient up to some distance from the inlet section and gradually decreases to minimum at the outlet section. The C_{tp} is high due to more vortices formation in the flow near to the absorber plate wall and obstruction offered by corrugation as shown in Fig. 7.17 (a), (b) and (c). The pressure drop occurs for the different geometries of the absorber plate were obtained and found to be maximum for the SAH having V-grooves corrugation on the absorber plate (P/e_v= 0.834) (shown in Fig. 7.17(c)).

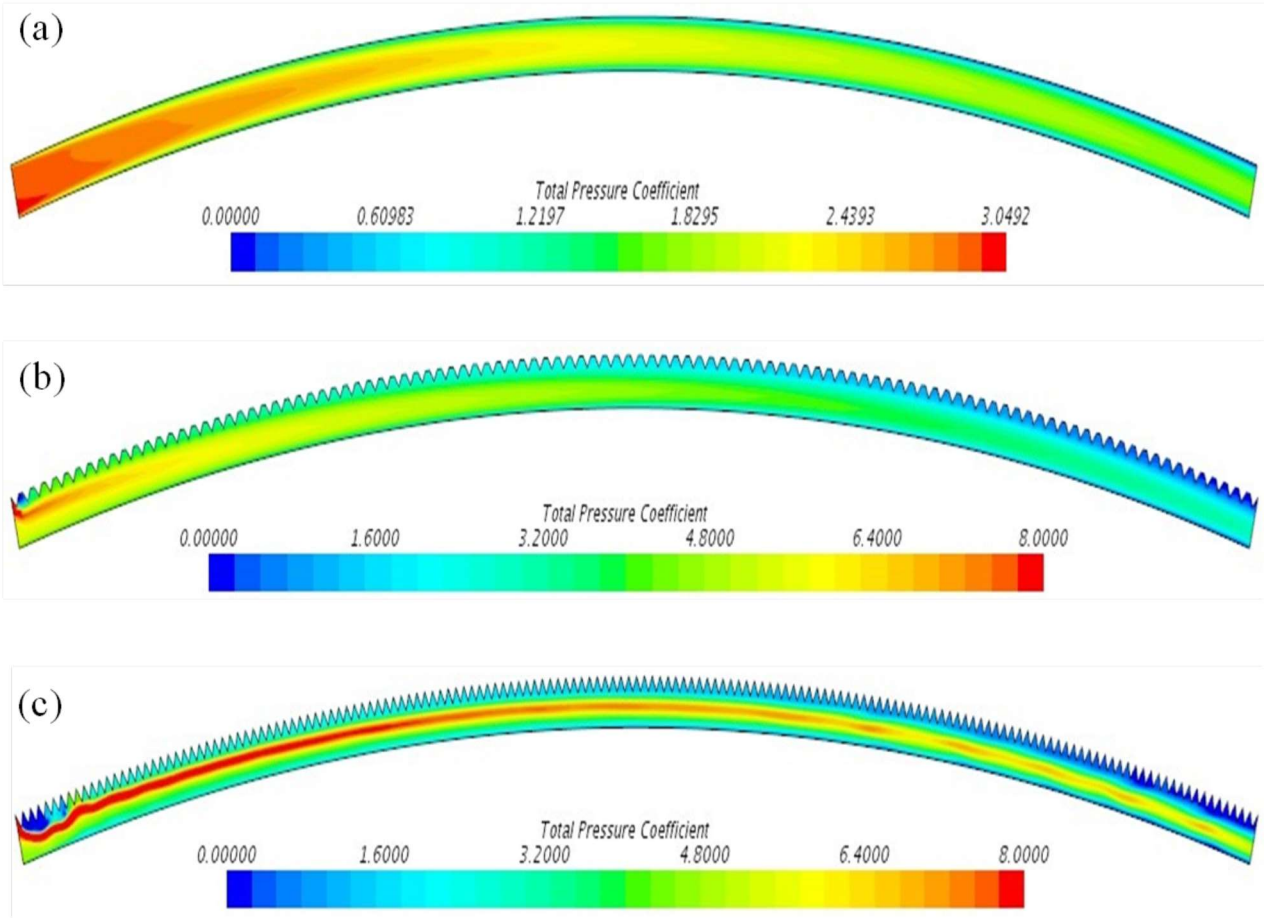

Figure 7.17: (a), (b) and (c) Total pressure coefficient for different geometries of curved SAH at mass flow rate of 0.0472 kg/sm^2. (a) Total pressure coefficient of CPSP SAH, (b) Total pressure coefficient of CPVCSP SAH (P/e = 1.25), (c) Total pressure coefficient of CPVCSP SAH (P/e = 0.834).

The turbulent kinetic energy is an important characteristic to understand thermal performance. Simulation results for turbulent kinetic energy have been obtained numerically for all SAH geometries. The maximum value of turbulent kinetic energy is for CPVCSP SAH having relative pitch ratio of P/e = 0.834 and next maximum for P/e = 1.25 at mass flow rate of 0.0472 kg/sm^{2}is shown in Fig. 7.18 (a) and (b). The value of turbulent kinetic energy is maximum near to tip of the V-grooves of the hot corrugated convex shape absorber plate. The turbulent kinetic energy indicates the magnitude of energy possess by the eddies in the turbulent flow region. High energy content in the eddies enhances the turbulence intensity which results in intense mixing of air in the flow accompanied with the higher heat transfer rate near to the hot absorber plate wall. Eddies possess more amount of turbulent kinetic energy which is derived from the mean flow in the convex shape flow passage of curved SAH.

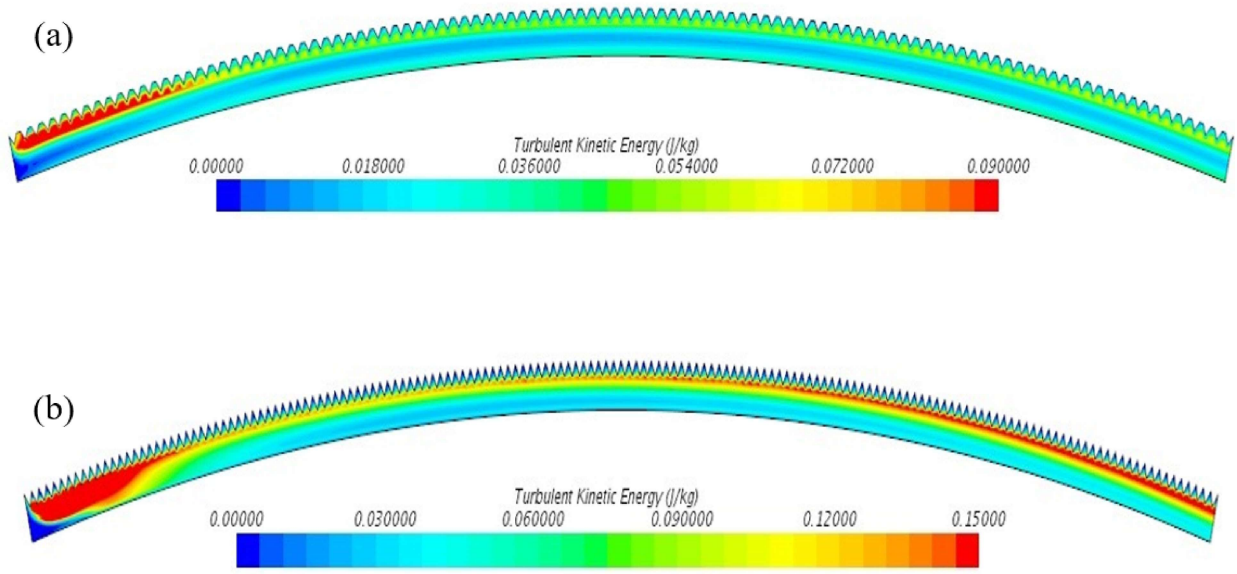

Figure 7.18: Turbulent kinetic energy contours of V-corrugated SAH at mass flow rate of 0.0472 kg/sm^2. (a) Turbulent kinetic energy of CPVCSP SAH (P/e = 1.25), (b) Turbulent kinetic energy of CPVCSP SAH (P/e = 0.834).

7.6 Correlation for Nusselt number and friction factor

As per results discussed in above section, it has been seen that Nu and f shows strong dependency over Reynolds number (Re), relative height ratio (e/H) and relative pitch ratio (P/e) of grooves. Relationships of these parameters with Nu and f can be written as,

$$Nu = F_1\,(Re,\ P/e,\ e/H) \tag{7.17}$$

$$f = F_2\,(Re,\ P/e,\ e/H) \tag{7.18}$$

The relationship between Nusselt number and Reynolds number results in power law in the form given below:

$$Nu = A_o\ Re^n \tag{7.19}$$

In order to obtain the relationship between Nusselt number and Reynolds number, variation of ln(Nu) verses ln(Re) for different values of relative height and relative pitch ratios of the grooves of absorber plate have been shown in Fig. 7.19. A linear relation has been observed between ln(Nu) and ln(Re) using all data point of SAH. Hence, logarithmic form of equation Nu = A_oRe^n can be written as:

$$ln\,(Nu) = ln\,(A_o) + n\,ln\,(Re) \tag{7.20}$$

A linear curve plot fitted with R-square method has been obtained is given below:

$$ln\,(Nu) = A_1 + 0.8102\,ln\,(Re) \tag{7.21}$$

Where, $A_1$is antilog of A_o and 'n' is exponent.

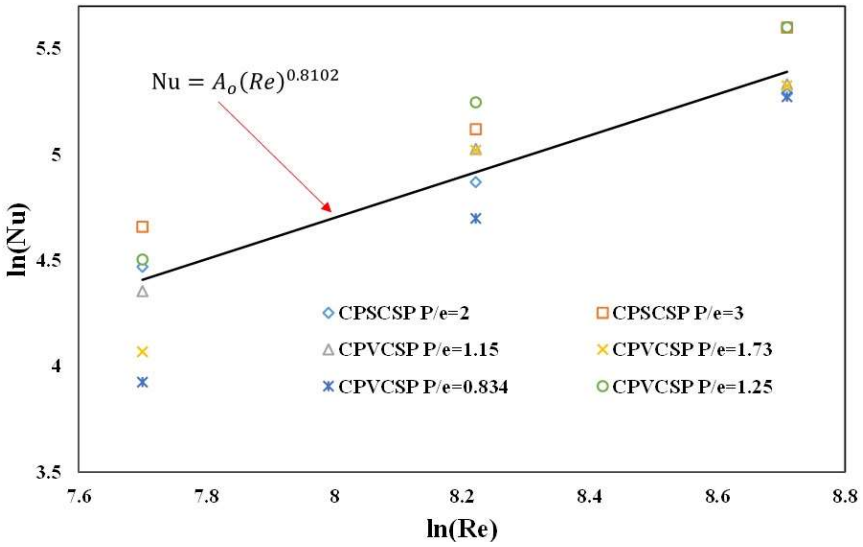

Figure 7.19: Plot of ln(Nu) verses ln(Re) of curved SAH having corrugated absorber plate.

Taking antilog of Eq. 7.21, we have,

$$Nu = A_o\,(Re)^{0.8102} \tag{7.22}$$

Coefficient A_o is a function of relative height and relative pitch ratios of grooves.

To get the relation between ln(A_o) with respect to ln(P/e) in linear trend can be written as follows;

$$ln\,(A_o) = ln\,(B_o) + m\,ln\,(P/e) \tag{7.23}$$

A linear trend observed in plot has been obtained using all the data point is shown in Fig. 7.20 and the equation obtained as;

$$ln\,(A_o) = ln\,(B_o) + 0.1733 ln\,(P/e) \tag{7.24}$$

After taking antilog,

$$A_o = B_o\,(P/e)^{0.1733} \tag{7.25}$$

where coefficient $B_o = \left(\frac{Nu}{Re^{0.8102}(P/e)^{0.1733}}\right)$ is a function of relative pitch ratio of grooves.

The plot between ln(B_o) and ln(e/H) was used to obtain the final expression of the Nusselt number. A relationship in the form of second order polynomial has been found and same has given below:

$$ln\,(B_o) = ln\,(C_1) + b\,ln\,(e/H) + c\,\{ln\,(e/H)\}^2 \tag{7.26}$$

A composite second order polynomial curve has been shown in Fig. 7.21. A regression analysis was used to fit a curve is given below.

$$ln\,(B_o) = ln\,(C_1) + (-0.64)\,ln\,(e/H) + (-0.2399)\,\{ln\,(e/H)\}^2 \tag{7.27}$$

By taking antilog of Eq. 7.27,

$$B_o = C_o\ (e/H)\ \ exp\left[-0.2399\,\{ln\,(e/H)\}^2\right] \tag{7.28}$$

where C_o=0.12 i.e. the antilog of C_1

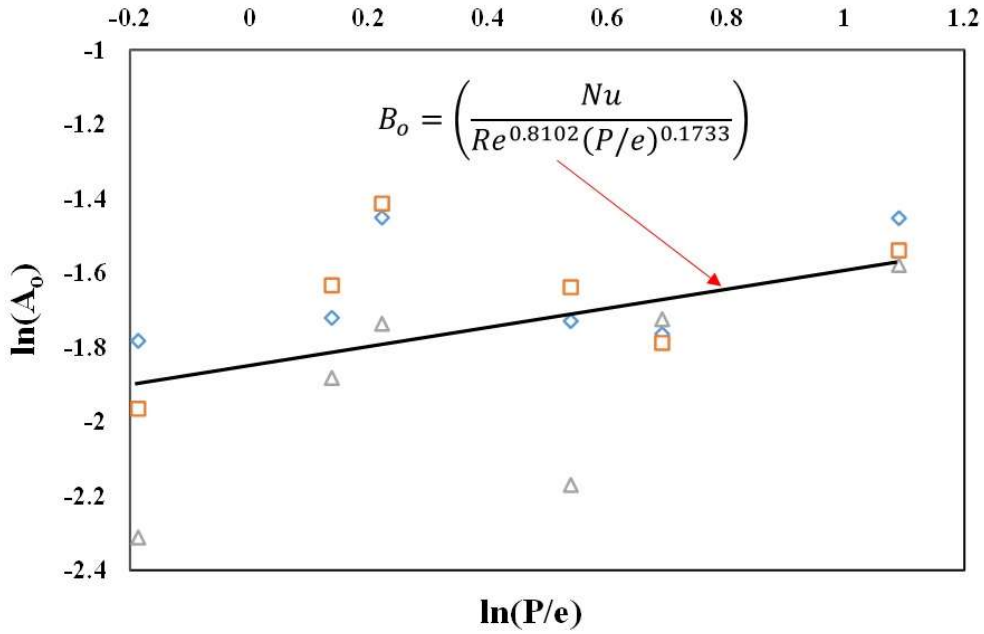

Figure 7.20: Plot of ln(Ao) verses ln(P/e) of curved SAH having corrugated absorber plate.

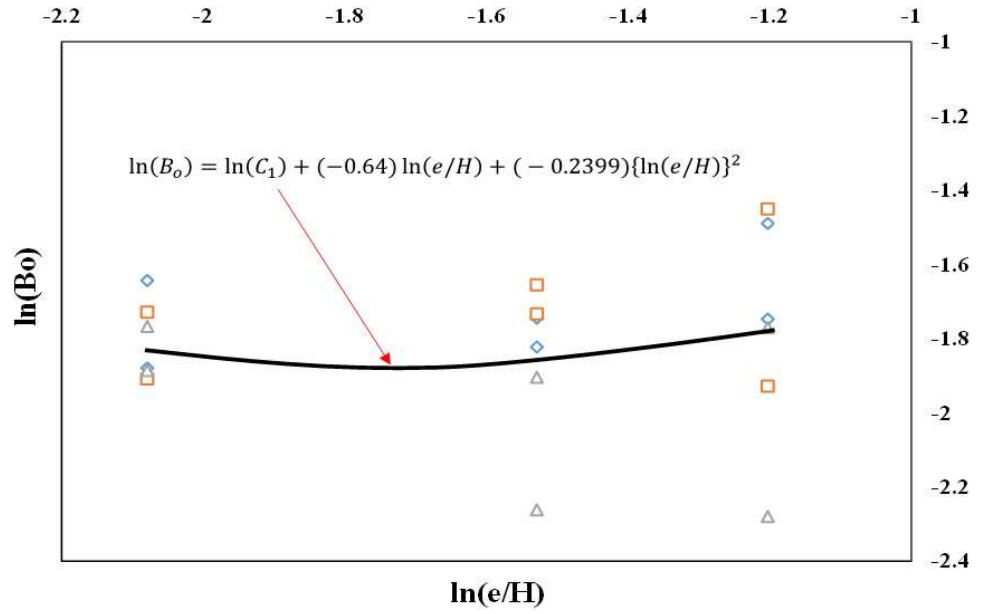

Figure 7.21: Plot of ln(Bo) verses ln(e/H) of curved SAH having corrugated absorber plate.

Rearranging Eq. 7.28

$$Nu = C_o \; Re^{0.8102} \;\; (P/e)^{0.1733} \, (e/H)^{-0.64} \;\; exp\left[-0.2399 \left\{ln\,(e/H)\right\}^2\right] \tag{7.29}$$

The above Eq. 7.29 is the final expression for the correlation of Nusselt number (Nu).

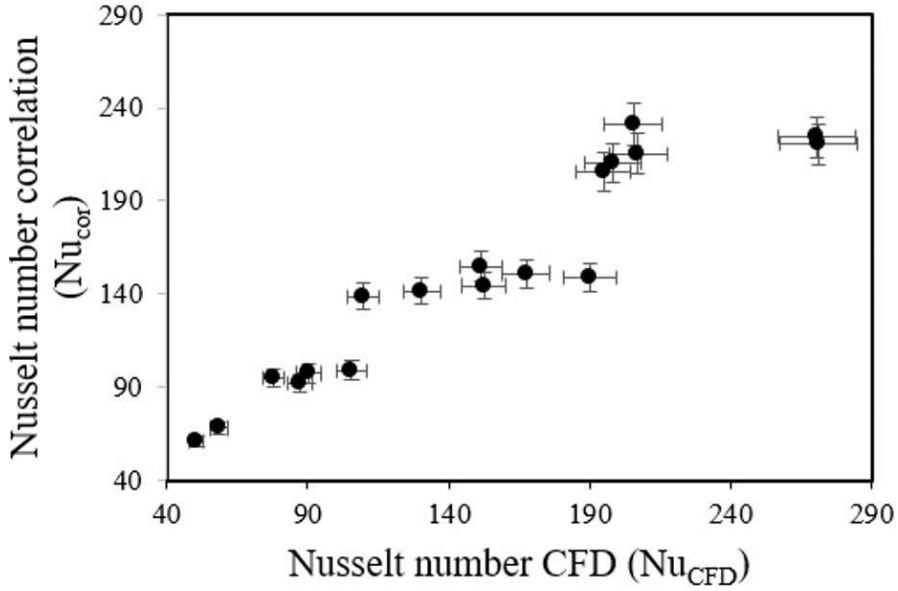

Figure 7.22: Comparison between values of Nusselt number correlation (Nu_{cor}) and Nusselt number CFD (Nu_{CFD}) of curved SAH having corrugated absorber plate.

The values of Nusselt number estimated by the correlation obtained above and CFD simulations have been compared and shown in Fig. 7.22. All data points of the correlation are in good agreement with the CFD results, having maximum percentage deviation of $\pm 13.42\%$.

Similarly, correlation of friction factor has also been obtained in terms of Reynolds number, relative height and relative pitch ratio of the grooves obtained using all data point is given below:

$$f = 6301.85 \; Re^{-0.4022} \;\; (P/e)^{-0.422} \, (e/H)^{10.036} \;\; exp\left[3.056 \left\{ln\,(e/H)\right\}^2\right] \tag{7.30}$$

The values of friction factor estimated by the correlation and CFD simulations have been compared, shown in Fig. 7.23. All data points of the correlation are in good agreement with the CFD results, having maximum percentage deviation of $\pm 13.47\%$.

The correlations developed for Nusselt number and friction factor are valid only for the parameter whose values lies in the range of $0.125 \leq e/H \leq 0.3$ and $0.834 \;\leq P/e \leq 3$.

The range of percentage deviation for both Nusselt number and friction factor are in the acceptable limits and shows good agreement with the CFD values. So, these correlations can be used to determine the Nusselt number and friction factor with reasonable accuracy.

7.7 Conclusions

The numerical simulations have been carried out for different geometries of curved absorber plate to study the dynamic thermal performance of smooth (single and double pass mode) and effect of different relative height and pitch ratios of semicircular groove and V-groove corrugation of the absorber plate of curved solar air heater. The effect of various designs of absorber plate on heat transfer characteristics i.e. Nusselt number, air outlet temperature and thermal efficiency were obtained. Correlations for the Nusselt number and friction factor are derived. The key aspects drawn from the results obtained in the present study are mentioned below:

1. Curved geometry of the smooth flow convex rectangular passage of the curved solar air heater proved to be more efficient than the flat plate solar air heater. Considerable increase in the air outlet temperature

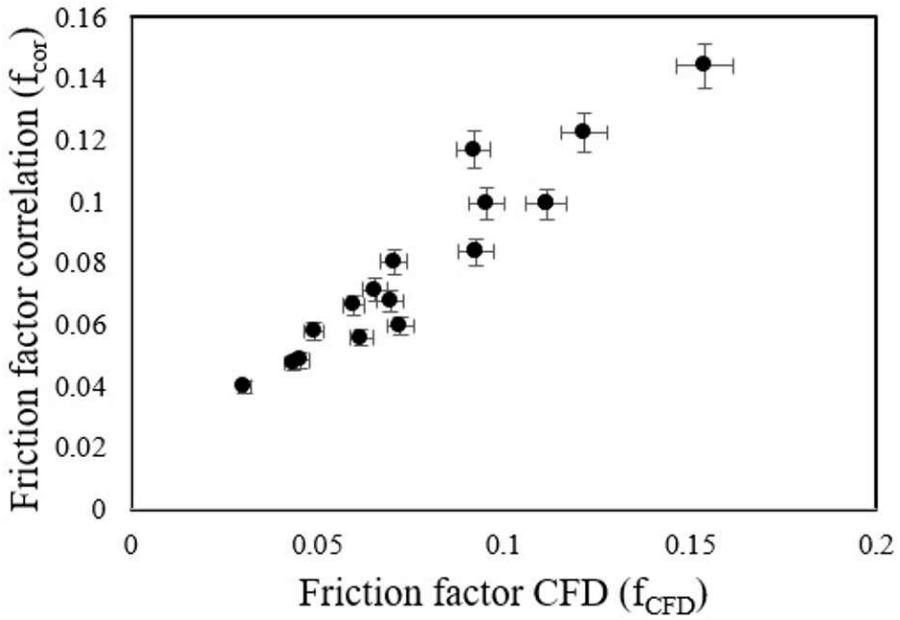

Figure 7.23: Comparison between values of friction factor correlation (f_{cor}) and friction factor CFD (f_{CFD}) of curved SAH having corrugated absorber plate.

and thermal efficiency have been seen for curved plate smooth single pass and double pass solar air heater compare to the flat plate smooth single and double pass solar air heater, respectively.

2. Increase in the relative height and pitch ratios of the corrugation of the absorber plate of curved solar air heater enhances the formation of secondary vortices which imparts more turbulence in air, results in intense mixing of air near to wall of the absorber plate. It provides scope of transferring more heat to the flowing air at larger values of mass flow rates compare to curved plate smooth solar air heater without corrugated absorber plate.

3. Maximum thermal efficiency of 91.93% has been seen for the solar air heater with curved plate V-corrugated single pass having P/e_v=0.834 and 32.05% percentage increase in the air outlet temperature with respect to curved plate smooth single pass solar air heater.

4. Pressure drop in case of absorber plate with corrugation has slightly more than the absorber plate without corrugation, as air flow obstructed by the corrugation of the absorber plate. Considerable increase in the thermal efficiency due to excess mixing of air which diminishes the drawback of slight increase in the pressure drop of curved solar air heater with corrugated absorber plate with respect to solar air heater without corrugated absorber plate.

5. Nusselt number for curved solar air heater varies as $Nu \sim C_o\ Re^a\ (P/e)^b\,(e/H)^c$ where a = 0.8102, b = 0.1733 and c = -0.64 in the range of parameters used. Data of Nusselt number and friction factor obtained by correlations under various conditions for different geometries of solar air heater were in good agreement with the data obtained by CFD.